Autonomously responsive pumping by a bacterial flagellar forest: A mean-field approach

James D. Martindale and Henry C. Fu

Autonomously responsive pumping by a bacterial flagellar forest: a mean-field approach

James D. Martindale and Henry C. Fu

Department of Mechanical Engineering, University of Utah, Salt Lake City, Utah, USA

(Dated: August 7, 2017)

This study is motivated by a microfluidic device which imparts a magnetic torque on an array of bacterial flagella. Bacterial flagella can transform their helical geometry autonomously in response to properties of the background fluid, which provides an intriguing mechanism allowing their use as an engineered element for the regulation or transport of chemicals in microscale applications. The synchronization of flagellar phase has been widely studied in biological context, but here we examine the synchronization of flagellar tilt, which is necessary for effective pumping. We first examine the effects of helical geometry and tilt on the pumping flows generated by a single rotating flagellum. Next, we explore a mean-field model for an array of helical flagella to understand how collective tilt arises and influences pumping. The mean-field methodology allows us to take into account possible phase differences through a time-averaging procedure and to model an infinite array of flagella. We find array separation distances, magnetic field strengths, and rotation frequencies that produce non-trivial self-consistent pumping solutions. For individual flagella, pumping is reversed when helicity or rotation is reversed; in contrast, when collective effects are included, self-consistent tilted pumping solutions become untilted non-pumping solutions when helicity or rotation is reversed.

I. INTRODUCTION

Advances in fabrication techniques for microfluidic devices utilizing biological and artificial flagella or cilia necessitate the development of methods to analyze how the flows are influenced by collective effects such as synchronization. Previous investigators have shown that oscillating synthetic cilia may be used to capture or release particles [1], change the flow direction within microchannel geometries [2], transport microparticles [3], and even regulate heat flow [4]. The collective motion of active or passive cilia may also be used to repel microswimmers [5] or particles [6] away from a surface, which has applications such as self-cleaning surfaces or enhancement of mixing. Synchronization of flagella or cilia direction and the phase of rotation or beating pattern is crucial for establishing transport. Synchronization of flagella has been achieved by biological systems in metachronal waves beating at the surface of *Volvox carteri* [7–9], and has been studied by examining the phase synchronization of eukaryotic flagella for biflagellates such as *Chlamydomonas* [10]. Collective tilting of nodal cilia in developing embryos is crucial in setting the left-right asymmetry of the internal organs, a phenomenon which has been examined experimentally [11] and numerically [12, 13]. Furthermore, extensive theoretical work has examined synchronization in a variety of models of varying simplicity. Hydrodynamic effects which lead to phase synchronization have been examined in minimalist numerical models such as a pair of paddles [14] or helices [15] acted on by a constant torque, or constant-force rotors used to model a bacterial carpet [16], as well as more complex models investigating fluid transport efficiency for metachronally beating magnetically actuated cilia [17].

Here we are motivated by a microfluidic device which utilizes bacterial flagella for magnetically actuated pumping (Fig. 1). In this "flagellar forest", bacterial flagella
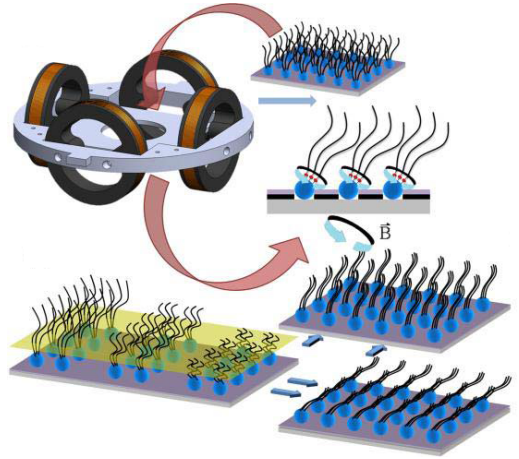

FIG. 1: The flagellar forest array within a Helmholtz coil system for 3D magnetic actuation (courtesy of M.J. Kim, BaST Lab, SMU).

are removed from *Salmonella typhimurium*, biotinylated, and fixed to streptavadin-coated magnetic microbeads via chemical bonding. The beads are deposited onto a glass substrate, and the flagellar forest array is placed in a three dimensional Helmholtz coil system which actuates the beads using a rotating magnetic field. The rotation of the beads imparts a torque onto the flagella, and their rotation creates a pumping flow. Bacterial flagella autonomously undergo transformations between polymorphic forms in response to changes in certain properties of the background fluid such as temperature, ionic concentration, or pH [18–20], which creates a natural mechanism for self-regulation that is of particular interest in laboratory applications [21, 22]. For example, the flagellar forest could be included as a thermoregulatory element in a larger system – if heating raises the ambi-

ent temperature of the fluid above a certain threshold it could induce a polymorphic transformation which in turn changes the pumping characteristics of the flagella. This transformation could cause an increase in flow rate, thereby dissipating heat and returning the system to its original temperature. In order to model a microscale device such as the one shown in Fig. 1, we will define a magnetic moment $\mathbf{m}$ which lies on the substrate at the base of the flagellum and is free to rotate along with the flagellum. A rotating external magnetic field $\mathbf{B}$ with rotational frequency ω is prescribed and creates a torque $\mathbf{N} = \mathbf{m} \times \mathbf{B}$ which drives the flagellum in a background flow. In such a device, the direction and magnitude of the pumping flow is dependent on the synchronization of the tilt angle of the flagella.

It is important to note that the magnetic actuation and our emphasis on tilt synchronization in these microscale devices differs from previous experimental and numerical studies performed in modeling the dynamics and coordination of bacterial carpets and arrays of bacterial flagella actuated by flagellar motors of live bacteria on a substrate [23–26], which highlight the effect of various geometric assumptions on the resulting flow field and focus on phase synchronization. Experimentally, Darnton *et al.* [23] fixed bacteria to a substrate so that their flagella could freely rotate, driven by bacterial motors which transmit a nearly constant torque to the flagella over their range of natural rotation rates [27]. It was shown that if the flagella remained upright, "whirlpool" type flows were observed in a plane parallel with the substrate and above the flagella. Uchida and Golestanian [16, 24] studied the phase synchronization of rotors with random intrinsic frequency as a basic model of a bacterial carpet, and used a mean-field approach to show that collective motion is acheived only for a very narrow distribution of intrinsic frequency. Buchmann *et al.* [26] performed numerical simulations using a 4×4 regular array of helices to show that small random tilt angles and random phase differences between helices not only reproduce experimental results when the helices are upright, but may also produce observed "river" type transport for small tilt angles. In the numerical simulations of Buchmann *et al.*, the tilt and phase angles were prescribed along with a direction and magnitude of rotation, so the synchronization of tilt angles could not be studied.

Buchmann *et al.* emphasized that random phase differences between flagella play a crucial role in creating flow properties one would observe in a micro-scale pumping setting. One drawback of such direct numerical studies is that the flagellar array is taken to be finite and small so that full numerical simulation is tractable. Other studies examine infinite flagellar arrays using doubly periodic solutions to the Stokes equation [25], but these necessitate the use of prescribed phase differences over some finite sized domain to be infinitely duplicated in each direction. The various constraints in these studies show the need for a method which enables us to study the collective tilting effects of large carpets of geometrically realistic flagella

while incorporating random phase differences. In this paper, we first address the effects of helical geometry, handedness, and tilt on pumping due to a single rotating flagellum. We then examine synchronization of tilt angle – which plays a crucial role in microscale pumping – for an infinite, regular, two dimensional array of flagella, using a mean-field approach to classify pumping stability while averaging over phase differences between flagella. This methodology allows us to compare and contrast the collective effects of tilt and handedness on pumping with those of a single flagellum.

II.   HYDRODYNAMIC MODEL

In microscale pumping applications, typical Reynolds numbers are in the range of $10^{-5} - 10^{-7}$ for which hydrodynamics are governed by the equations of incompressible Stokes flow,

$$\mu \nabla^2 \mathbf{u} - \nabla p = 0$$
$$\nabla \cdot \mathbf{u} = 0, \tag{1}$$

where μ is viscosity, $\mathbf{u}$ is the fluid velocity, and p the pressure. The Stokeslet is a fundamental solution to the Stokes flow equations, corresponding to a velocity field induced by a point force $\mathbf{f}$ at $\mathbf{x_0}$

$$8\pi\mu u_i(\mathbf{x}) = S_{ij}(\mathbf{x}, \mathbf{x_0}) f_j \tag{2}$$

$$S_{ij} = \frac{\delta_{ij}}{r} + \frac{(\mathbf{x} - \mathbf{x_0})_i (\mathbf{x} - \mathbf{x_0})_j}{r^3}, \tag{3}$$

where S_{ij} is called the Stokeslet kernel, δ_{ij} is the Kronecker delta, and $r = |\mathbf{x} - \mathbf{x_0}|$.

In the flagellar forest, the glass substrate above which the flagella rotate is a no-slip boundary. Above a no-slip plane, the contribution of the Stokeslet plus an image system – termed the Blakelet – is a fundamental solution to Eq. 1 [28, 29], corresponding to a velocity field

$$8\pi\mu u_i(\mathbf{x}) = B_{ij}(\mathbf{x}, \mathbf{x_0}) f_j \tag{4}$$

where B_{ij} is called the Blakelet kernel. The velocity field due to the Blakelet singularity can be found in Eq. 8 in Blake and Chwang [29].

For numerical simulations in Stokes flow, we use the method of regularized Stokeslets with the appropriate image system [30–33] to enforce no-slip conditions on the plane boundary $x_1 = 0$. In this method, unknown point forces along the flagellum are regularized by replacing the Dirac δ-function with a 'blob' function described by

$$\phi^\epsilon(\mathbf{x} - \mathbf{x_0}) = \frac{15\epsilon^4}{8\pi(r^2 + \epsilon^2)^{7/2}}, \tag{5}$$

where $\epsilon \ll r$ is a parameter which controls the spatial extent of the force and $\int \phi^\epsilon(\mathbf{x}) \, d\mathbf{x} = 1$. For this choice

of blob, the regularized Stokeslet kernel becomes

$$S_{ij}^\epsilon(\mathbf{x}, \mathbf{x_0}) = \frac{\delta_{ij}(r^2 + 2\epsilon^2) + (\mathbf{x} - \mathbf{x_0})_i(\mathbf{x} - \mathbf{x_0})_j}{(r^2 + \epsilon^2)^{3/2}} \quad (6)$$

and we define the full regularized Blakelet kernel as B_{ij}^ϵ. Details of this kernel along with the velocity field due to the regularized Blakelet are found explicitly in Eq. 21 of Ainley *et al.* [32] and our implementation in Martindale *et al.* [34] Note that in the limit $\epsilon \to 0$, the regularized kernels reduce to the classical singular kernels.

The flagella used in our model are rigid helices of filament radius a, helical radius R, helical pitch p, helical arc length L, and chirality (handedness) $\chi = \pm 1$, with a tapering region described by the tapering parameter $k_E = p/(2\pi)$ such that the connection point with the $x_1 = 0$ plane lies at $(x_2, x_3) = (0,0)$. In lieu of explicitly modeling the magnetic microbeads, helices are translated to a height $h = 10a$ above the no-slip plane. For example, the centerline parameterization of an helical filament aligned with the $\hat{\mathbf{e}}_1$-axis is described by [33]

$$\mathbf{r_c}(s) = (h+s)\hat{\mathbf{e}}_1 + \left(1 - e^{-s^2/k_E^2}\right) R\Big[\cos(2\pi s\chi/p)\hat{\mathbf{e}}_2$$
$$+ \sin(2\pi s\chi/p)\hat{\mathbf{e}}_3\Big] \quad (7)$$

where $\{\hat{\mathbf{e}}_1, \hat{\mathbf{e}}_2, \hat{\mathbf{e}}_3\}$ is an orthonormal basis. We prescribe the helical geometry for each polymorphic form using the measurements from Hasegawa *et al.* [20] For example, in Table I we show the helical radius and pitch of the normal (n=2) and curly (n=5) forms. These two forms are selected since they are the most commonly observed forms as pH and ionic strength are varied [19]. While a complete flagellar forest has not yet been fabricated, when single or a few flagella are observed attached to a substrate, they are nearly always observed in one of these two forms [35].

TABLE I: The helical geometry of the normal and curly polymorphic forms

Polymorphism number n	Helical Radius (μm)	Helical Pitch (μm)
2	0.196	2.233
5	0.156	1.361

In our model, N regularized Stokeslets are distributed at collocation points $\mathbf{x}^\alpha$ along the centerline of the flagellum $\mathbf{r_c}(s)$, which we have shown to give accurate results for slender filaments such as bacterial flagella [34]. The flow due to the helix is written as

$$8\pi\mu u_{helix,i}(\mathbf{x}) = \sum_{\alpha=1}^N B_{ij}^\epsilon(\mathbf{x} - \mathbf{x}^\alpha)f_j^\alpha. \quad (8)$$

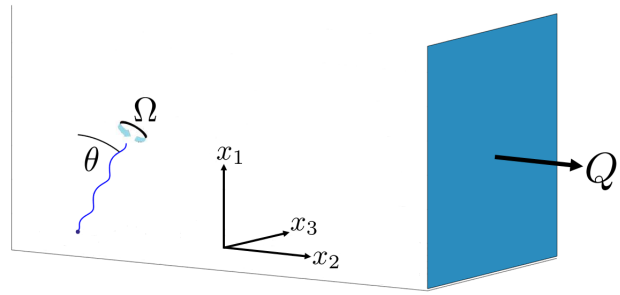The regularized Blakelet kernel in this formula ensures that the contribution from the helix will satisfy no-slip

FIG. 2: Diagram of a single flagellum with tilt θ and rotation rate Ω. The vertical plane in blue is an infinite upper half-plane through which the flux Q is calculated.

conditions on the plane $x_1 = 0$. For the normal (n=2) and curly (n=5) polymorphic forms of bacterial flagella examined here we have used the Stokeslet spacing and blob parameters described in Martindale *et al.* [34] This centerline distribution with optimal parameters greatly reduces the computational time needed to accurately model the dynamics of the flagella.

III. PUMPING DUE TO A SINGLE FLAGELLUM

To understand the pumping flows generated by a single flagellum rotating above a no-slip plane, we prescribe a tilt angle θ from the axis normal to the plane along with a constant rotation rate Ω in a clockwise direction about the helical axis. For each of the 10 helical polymorphic configurations [20], we create a flagellum with helical length $L = 7.1$ μm, filament radius $a = 0.00169\,L$, and tilt angle θ as seen in Fig. 2.

We calculate the time-averaged volumetric flow rate through an arbitrary vertical plane $P = \{\mathbf{x} \in \mathbf{R}^3 \mid x_1 > 0,\ x_2 = C\}$ by averaging over one rotational period the instantaneous volumetric flow rate, which due to the linearity of the Stokes flow equations can be written as a sum of the volumetric flow rate due to each regularized Blakelet [12, 21, 36],

$$Q = \sum_{\alpha=1}^N \frac{x_1^\alpha\, f_2^\alpha}{\mu\pi}. \quad (9)$$

For each helical polymorphic form, we calculate the non-dimensionalized volumetric flow rate $\tilde{Q} = Q/|\Omega|L^3$ for tilt angles $0° \leq \theta \leq 60°$ (since after a $60°$ tilt angle many forms intersect with the $x_1 = 0$ plane) and plot the results in Fig. 3. We note that the maximum volumetric flow rate is achieved for each polymorphic form for a tilt angle of approximately $45°$. We have found that not only does the pumping magnitude vary greatly depending on polymorphic form, but that left and right handed helical forms produce pumping in opposite direc-
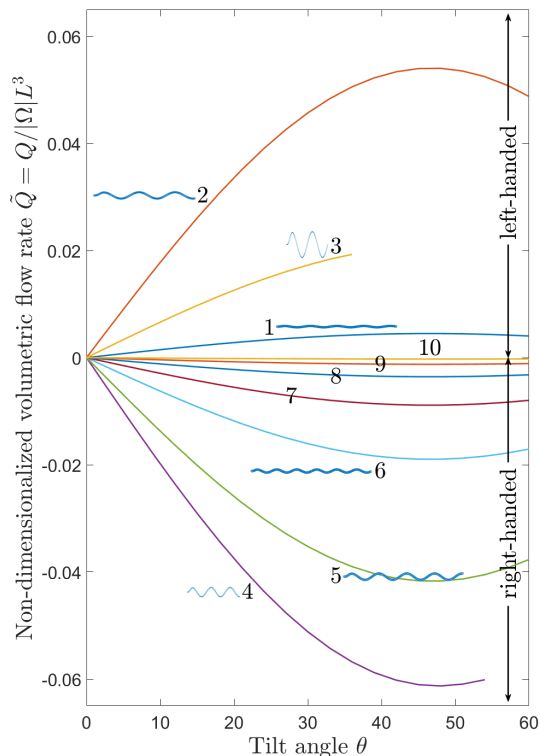
FIG. 3: Non-dimensionalized volumetric flow rate over one rotational period for the 10 helical bacterial polymorphic forms as a function of tilt angle θ. Rotational direction is clockwise about the helical axis.

tions, an important feature in autonomously regulated pumping. Recalling our example from Sec. I, this result suggests that inducing a polymorphic transformation by the introduction of a heat source could cause a reversal of flow which aids the dissipation of heat and acts as a mechanism for the self-regulation of a system.

In the rest of the paper, we concentrate on the normal (n=2, left-handed) and curly (n=5, right-handed) forms since those are the most commonly observed forms during the development of flagellar forests. As single flagella, they pump in opposite directions, but in a forest the presence of additional flagella complicates matters due to the hydrodynamic interactions between them. Once hydrodynamic interactions are included, we cannot prescribe the rotation rate and axis, so instead we remove these constraints to model the magnetic torque which drives the flagella in our microfluidic device. As the number of flagella grows, it becomes increasingly difficult to model the hydrodynamic interactions in order to examine collective effects of tilt on pumping. Next, we attempt to address how collective effects and interactions alter the conclusions based on a single flagellum.
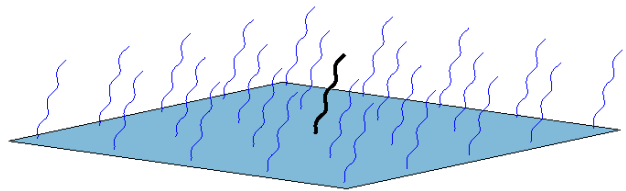

FIG. 4: A regular $D \times D$ array of helical flagella, show here with equal tilt angle and phase. The central helix is colored black and made bold solely for emphasis in the mean-field methodology.

IV. MEAN-FIELD METHODOLOGY

To examine collective tilting of bacterial flagella, we consider a regular array of helices as seen in Fig. 4 to model a microscale pumping device such as the one in Fig. 1. The size of a $D \times D$ array will be called D, and the separation distance between flagella is d. Hydrodynamic interactions between flagella can promote collective tilting since a tilted flagellum indues a flow in the direction of the tilt, which pushes nearby flagella to also tilt in the same direction. In principle each flagellum may have a slightly different tilt angle, but in a mean-field approach [37], we ignore these fluctuations and assume that due to symmetry each flagellum behaves identically with the same tilt angle and experiences an identical background flow caused by all other flagella in the array. The goal is to find the flagellar configuration (tilt angle) such that it produces a background flow that leads to that same tilt angle, i.e. self-consistency. Therefore without loss of generality, we choose to focus on the central helix, whose base lies at the standard origin (colored black in Fig. 4).

The central helix is acted on by a background flow $\mathbf{U}_\infty(\mathbf{x})$ which we imagine is due to all the other helices in the array, as well as an external magnetic torque $\mathbf{N} = \mathbf{m} \times \mathbf{B}$ where $\mathbf{m}$ is a magnetic moment located at $\mathbf{x} = \mathbf{0}$ that takes a fixed orientation relative to the helix, i.e. it rotates and tilts with the helix, and $\mathbf{B}$ is a rotating magnetic field described by

$$\mathbf{B} = B_0 \left(0, \cos \omega t, \sin \omega t\right). \qquad (10)$$

We represent the full flow field as $\mathbf{u}(\mathbf{x}) = \mathbf{u}_{helix}(\mathbf{x}) + \mathbf{U}_\infty(\mathbf{x})$ where $\mathbf{u}_{helix}(\mathbf{x})$ is given by Eq. 8 and $\mathbf{U}_\infty(\mathbf{x})$ is the background flow. Note that $\mathbf{u}_{helix}(\mathbf{x}) \to \mathbf{0}$ as $r = |\mathbf{x}| \to \infty$ and $\mathbf{u}_{helix}(x_1 = 0) = \mathbf{0}$. In order for no-slip conditions to be met for the full velocity field, we further require that $\mathbf{U}_\infty(x_1 = 0) = \mathbf{0}$. In the mean-field model the base of the helix does not translate. We solve for the unknown force at the base of the helix as well as its rotation.
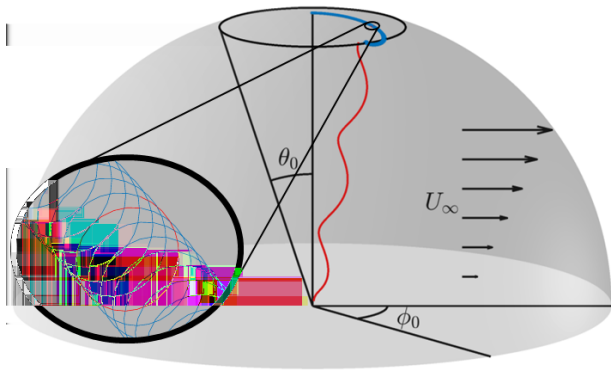
FIG. 5: An example of the epicyclic motion of the helical axis on a unit sphere and the convergence to a stable orbit about $\{\theta_0, \phi_0\}$ for a background shear $\mathbf{U}_\infty(\mathbf{x}) = \dot{\gamma} x_1 \hat{\mathbf{x}}_2$. Scaled helix at final position shown in red. Inset: a highlighted epicycle to show helical dynamics.

FIG. 6: The self-consistent nondimensionalized y-component of the shear-like velocity profile $\mathbf{U}_\infty(\mathbf{x})$ induced on the central helix by all other helices in the array versus the normalized arc length for Mason number $\mathrm{Ma} = \mu \omega R^3 / |\mathbf{m}||\mathbf{B}| = 3.32 \times 10^{-3}$ and array separation distance $d = L$.

V. ROTATING HELIX IN BACKGROUND FLOW

The dynamic motion of a helix embedded in a background flow and driven by a torque from a rotating magnetic field is interesting in and of itself, and helps to understand the results of the mean-field approach. To illustrate the typical dynamics, we choose a simple background shear flow $\mathbf{U}_\infty(\mathbf{x}) = \dot{\gamma} x_1 \hat{\mathbf{x}}_2$. As the magnetic field rotates in the $x_1 = 0$ plane, the helical axis undergoes small epicyclic orbits (inset in Fig. 5) with the same rotational period T as the magnetic field while its orientation is influenced by the background flow.

The rotating magnetic field $\mathbf{B}$ causes a torque on the magnetic moment $\mathbf{m}$ at the base of the helix which is balanced by the hydrodynamic torque induced by drag from the motion of the helix through the fluid. If the field rotation rate ω is slow enough, the magnetic moment of the bead $\mathbf{m}$ will have a constant lag angle behind the magnetic field $\mathbf{B}$, and the motion of the helix will be steady and rotate with the field [38]. However, if ω is too large, the angle between the magnetic moment $\mathbf{m}$ and the magnetic field $\mathbf{B}$ will become unsteady, and the motion of the helix will no longer be synchronized with the magnetic field rotation. The critical frequency ω^* below which we have steady rotation is called the step-out frequency of the helix, and is determined by the magnetic moment as well as the helical geometry. If the rotation rate of the magnetic field is below ω^*, the epicyclic motion of the helix converges to a stable orbit about an axis described by the tilt and azimuthal angles $\{\theta_0, \phi_0\}$, seen in Fig. 5.
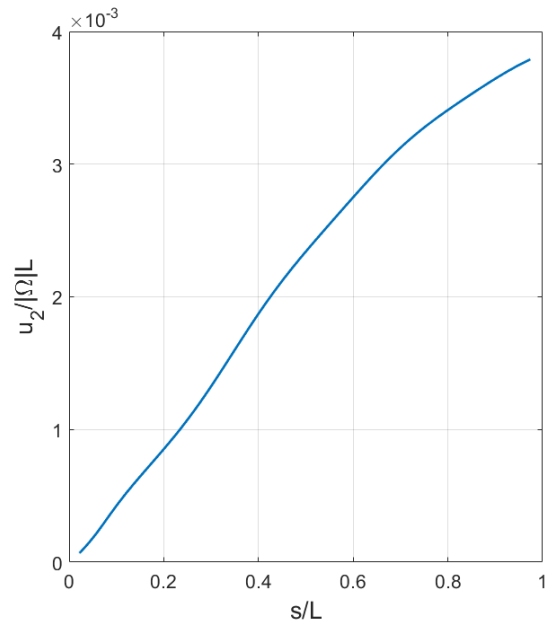
VI. MEAN-FIELD CALCULATION AND PRECESSION

In the mean-field approach, the background flow $\mathbf{U}_\infty(\mathbf{x})$ is caused by all the helices in the array except the central helix. The numerical method finds the forces and positions of the collocation points on the central helix. Assuming that every helix in the array has the same force distribution, we calculate a new background flow at the central helix as the sum of the time-averaged flows produced by all other helices in the array. Note that polymorphic transformations typically occur on the timescale of 10 ms [39], while rotational frequencies are typically from 1-50 Hz, so here we consider any transformations to be instantaneous and the flagellar geometry to be fixed throughout the calculation. As detailed in Secs. VI A and VI B, this induces a new flow field $\mathbf{U}_\infty(\mathbf{x})$ (usually quite shear-like in profile as seen in Fig. 6), and we recalculate the behavior of the central helix in this new flow, again driven by a magnetic torque at its base. After one period, this process is repeated until a self-consistent solution is found, i.e. the tilt angle of the helix produces the background flow required to obtain that tilt angle. Because the flow is found by time-averaging over one rotational period, this process is similar to using random phase differences in a direct numerical simulation to find the velocity field, repeating this simulation many times, and then averaging over these velocity fields.
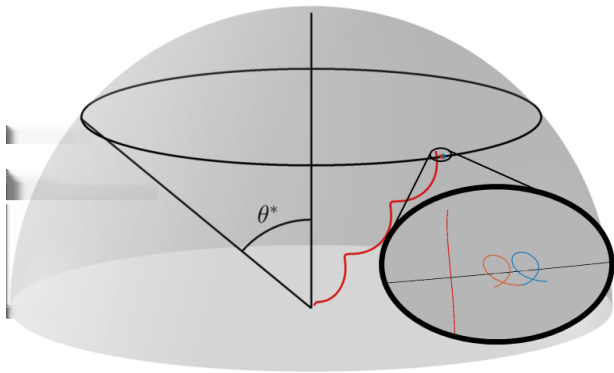
FIG. 7: An example of precessional pumping motion for a pumping angle θ^*. The direction of precession is clockwise (the same direction as the rotating magnetic field **B**). Inset: epicycles with circles drawn through their average helical axis about the x_1-axis.

In the example using a background shear flow, we saw that the azimuthal angle ϕ_0 of the stable orbit did not align with the direction of the background flow. This is reminiscent of the chiral flows tangent to the edge of a bacterial swarm produced by flagella extended radially out of the edge [40]. Calculating the background flow using the time-averaged forces found during this orbit results in a shear-like background flow $\mathbf{U}_\infty(\mathbf{x})$ at the central helix in the direction of ϕ_0. However, in such a background flow the helix again has a stable orbit which is not aligned with the new flow. Therefore under continuous rotation by magnetic torque, the helix and the resulting background flow precess, with the azimuthal angle ϕ steadily increasing in time.

Therefore, rather than requiring $\{\theta, \phi\}$ to stay the same for self-consistency, if we find a tilt angle θ^* for which we observe perfect precessional motion of the central helix from one period to the next, we say that this configuration is self-consistent. This is accomplished by fixing the azimuthal angle at ϕ_0 and searching over a range of tilt angles θ for epicycles which produce an average helical axis which is a pure rotation about the $\hat{\mathbf{x}}_1$ axis from one period to the next. We define $\Delta\theta$ as the difference in tilt angles of the average helical axes for two consecutive epicycles so that our problem is a search for a tilt angle θ^* for which $\Delta\theta = 0$ and $\Delta\phi$ is constant. With this definition, a self-consistent solution corresponds to pumping (see below), but because of the precessional motion, the pumping direction constantly rotates. One such example of a configuration for which we find a stable pumping angle is seen in Fig. 7. On the other hand, if we observe that the central helix always tends toward upright, there is no net pumping flow.

Physically we interpret precessional self-consistency as pumping since we believe that wall effects in confined microchannel geometries used in microfluidic devices such as the flagellar forest (Fig. 1) set a preferred geometry which confines the flow and results in a stable pumping angle. We confirm this intuition in Sec. VII A by adding a vertical slip wall to our calculation, which selects a single self-consistent direction and removes precession. In the following subsections we detail how the time-averaged background velocity is calculated for an infinite array, then present results for self-consistent stability of pumping.

A. Time-averaged velocity induced on a flagellum

Consider the central flagellum with centerline $\mathbf{r_0}(s,t)$ made of collocation points $\mathbf{x_0}^{\alpha_1}(t)$ for $\alpha_1 = 1, ..., N$, along with another helix with centerline $\mathbf{r_1}(s,t)$ with collocation points $\mathbf{x_1}^{\alpha_2}(t)$ for $\alpha_2 = 1, ..., N$. To find the background flow $\mathbf{U}_\infty(\mathbf{x})$, we seek an expression for the time-averaged fluid velocity on the central helix induced by another helix undergoing periodic motion with period T. With helices such as bacterial flagella where the length is much larger than the helical radius [$L/R \approx 36$ for the normal (n=2) form and $L/R \approx 45$ for the curly (n=5) form], we may perform an expansion in this small radial component.

To accomplish this, we treat each helix as a straight, rod-like, time-independent component in the direction of the average helical axis over an epicycle plus a small time-dependent component which captures the helical radius and rotational dynamics over an epicycle, i.e. $\mathbf{r_0}(s,t) = \mathbf{r_{0,rod}}(s) + \Delta\mathbf{r_0}(s,t)$. We then write the time-averaged velocity induced at one of the collocation points on $\mathbf{r_{0,rod}}(s)$, called $\mathbf{x_{0,rod}}^{\alpha_1}$ as

$$\overline{u_j}(\mathbf{x_{0,rod}}^{\alpha_1}) = \frac{1}{T}\int_0^T \sum_{\alpha_2=1}^N B_{jk}\left(\mathbf{x_0}^{\alpha_1}(t) - \mathbf{x_1}^{\alpha_2}(t)\right) f_k^{\alpha_2}(t)\,dt$$

(11)

where B_{jk} is the Blakelet kernel and $\mathbf{f}^{\alpha_2}(t)$ is the time-dependent force at the collocation point $\mathbf{x_1}^{\alpha_2}(t)$.

Assuming this time-dependent term $\Delta\mathbf{r_0}(s,t)$ is small, we expand the Blakelet kernel which appears in Eq. 11 as

$$B_{jk}\left(\mathbf{r_0}(s,t) - \mathbf{r_1}(s,t)\right) \approx B_{jk}\left(\mathbf{r_{0,rod}}(s) - \mathbf{r_{1,rod}}(s)\right)$$
$$+ \Delta\mathbf{r_0}(s,t)\frac{\partial B_{jk}}{\partial \mathbf{r_{0,rod}}}\left(\mathbf{r_{0,rod}}(s) - \mathbf{r_{1,rod}}(s)\right)$$
$$+ \Delta\mathbf{r_1}(s,t)\frac{\partial B_{jk}}{\partial \mathbf{r_{1,rod}}}\left(\mathbf{r_{0,rod}}(s) - \mathbf{r_{1,rod}}(s)\right).$$

(12)

Inserting this expression from Eq. 12 into Eq. 11 and

collecting time-dependent terms gives

$$
\overline{u_j}(\mathbf{x_{0,rod}^{\alpha_1}}) \approx \sum_{\alpha_2=1}^{N} B_{jk} \left(\mathbf{x_{0,rod}^{\alpha_1}} - \mathbf{x_{1,rod}^{\alpha_2}} \right) \left(\frac{1}{T} \int_0^T f_k^{\alpha_2}(t)dt \right)
$$
$$
+ \sum_{\alpha_2=1}^{N} \frac{\partial B_{jk}}{\partial \mathbf{r_{0,rod}}} \left(\mathbf{x_{0,rod}^{\alpha_1}} - \mathbf{x_{1,rod}^{\alpha_2}} \right) \left(\frac{1}{T} \int_0^T \Delta\mathbf{x_0^{\alpha_1}}(t) f_k^{\alpha_2}(t)dt \right)
$$
$$
+ \sum_{\alpha_2=1}^{N} \frac{\partial B_{jk}}{\partial \mathbf{r_{1,rod}}} \left(\mathbf{x_{0,rod}^{\alpha_1}} - \mathbf{x_{1,rod}^{\alpha_2}} \right) \left(\frac{1}{T} \int_0^T \Delta\mathbf{x_1^{\alpha_2}}(t) f_k^{\alpha_2}(t)dt \right)
$$
$$
(13)
$$

The time-dependent terms collected in parentheses are evaluated separately as the helix undergoes a rotational period of motion. We have verified that this approximation yields results with 5.5% error compared to the full time-dependent expression for relatively small separation distances, i.e. $d = L/2$, with the results becoming more accurate as the separation distance increases. More importantly, Eq. 13 averages over phase angle differences between helices, allowing us to take phase angle into account without explicitly dealing with it at each time step.

B. The infinite array extrapolation

To find the velocity induced on the central rod by a finite array of helices, we must sum a contribution like Eq. 13 over each helix in the array. Recall that these velocities are calculated using time-averaged quantities taken from the dynamics of only the central helix over one period, so this process of generating the array velocity occurs once per rotational period. In order to calculate the velocity field at the central flagellum due to an infinite array of flagella, we extrapolate the velocity field produced at the central flagellum by successively larger arrays. We utilize the far-field expression for the Blakelet singularity to obtain power law decay rates in the velocity field, and then fit the finite array data to this prescribed functional form.

The details of the far-field decay rates due to a finite array of helices along with the calculation of the appropriate array size D needed to form an infinite array extrapolant are found in the Appendix. We find that extrapolating infinite array results from the calculated velocity components of arrays with size 11×11 and 17×17 produce accurate results while still allowing for relatively fast computation time.

VII. RESULTS

We use the mean-field methodology to find self-consistent pumping solutions for a variety of magnetic field rotation rates ω and array separation distances d. In this study, we prescribe a geometry for the normal (n=2) and curly (n=5) polymorphic forms of bacterial flagella,

both of helical arc length $L = 7.1$ μm and filament radius $a = 0.00169$ L. As mentioned in Sec. II, these two polymorphic forms are chosen as representative examples of the mean-field methodology because they are common in biological scenarios such as the run-and-tumble motion of bacteria and are forms most often observed in experiments using flagella attached to beads [41]. In Fig. 3, we showed that when considering a single flagellum, these forms produce a volumetric flow in opposite directions for the same rotation rate and helical axis due to the normal and curly forms having opposite chirality. Similarly, reversing the direction of rotation would reverse the pumping direction for each form.

In the mean-field methodology, the self-consistent orbit of a polymorphic form about θ_0 depends on the Mason number, $\text{Ma} = \mu\omega R^3/|\mathbf{m}||\mathbf{B}|$, a ratio of fluid to magnetic torque [42, 43]. If the Mason number is held constant for a given helical geometry, the behavior of the orbit will remain the same. For this reason, we present results in terms of the Mason number which incorporates experimental variations of both ω and $|\mathbf{B}|$. Including collective effects, for a clockwise rotation where the volumetric flow rate for an individual normal (n=2) flagellum is positive, we find stable self-consistent pumping solutions over a certain range of Mason numbers and helical separation distances d. On the other hand, for a counter-clockwise rotation of the normal form where the volumetric flow rate is negative for a single flagellum, there is no net pumping, and we find that the only self-consistent solution is the trivial case where the flagellum is oriented perpendicular to the no-slip plane. This can be rationalized since a background flow in the tilt direction is needed in order to stabilize the tilt angle. For the curly (n=5) form, where the flagellum has opposite handedness, the reverse is true – counter-clockwise magnetic field rotation produces a stable pumping solution, but clockwise rotation does not.

We report the self-consistent pumping angles in Fig. 8 for the normal (n=2) polymorphic form in a phase space of scaled Mason number $\text{Ma}/\text{Ma}_{\text{step-out}}$ and grid separation distance d, presented as a multiple of the helical length L for a clockwise rotational direction. X's show when self-consistent solutions are upright and produce no pumping. Pumping is possible for $0.5L \le d < 1.75L$, but requires a faster rotation rate as the array separation increases. We are not able to study pumping for $d < 0.5L$ since the assumptions used to derive Eq. 12 are violated, but based on the observed trend, the tendency seems to be that further decreasing the separation would lead to stronger hydrodynamic interactions, leading to more tilt and more pumping as long as the frequency is low enough. For $d > 1.75L$ we never observe collective tilting since the array becomes too sparse to produce pumping solutions. We note that the pumping angle θ^* decreases as the magnetic field rotation rate ω is decreased or the grid separation distance d is increased.

Since the chirality of the curly (n=5) form is opposite from the normal form, we must also reverse the direction
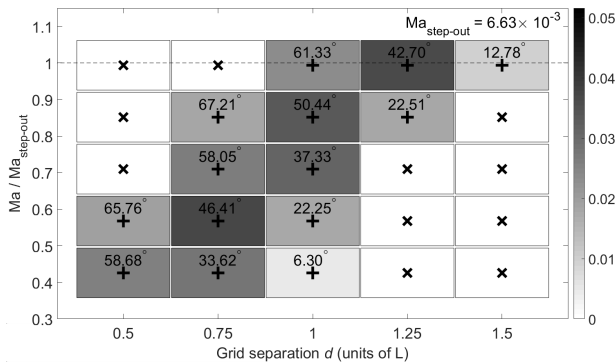
FIG. 8: Stable pumping angles θ^* in a phase space of scaled Mason number Ma/Ma$_{\text{step-out}}$ and grid separation distance d, normal (n=2) form, clockwise rotation. Patch faces are shaded by non-dimensional flow rate. "X" indicates self-consistent solution is upright (non-pumping). Counter-clockwise rotation always yields non-pumping behavior.
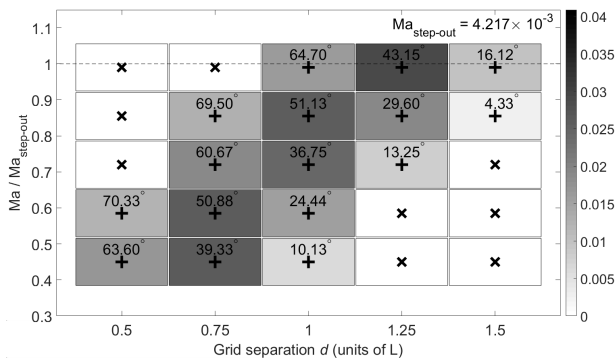

FIG. 9: Stable pumping angles θ^* in a phase space of scaled Mason number Ma/Ma$_{\text{step-out}}$ and grid separation distance d, curly (n=5) form, counter-clockwise rotation. Patch faces are shaded by non-dimensional flow rate. "X" indicates self-consistent solution is upright (non-pumping). Clockwise rotation always yields non-pumping behavior.

of the magnetic field rotation to observe self-consistent pumping angles. Self-consistent pumping angle for the curly form are shown in Fig. 9. Recall from Table I that the helical radius of the curly form is smaller than that of the normal form, however, this implies that for the same helical arc length L, the axial length of a helix in the curly form is longer than the normal form. The velocity field scales approximately linearly with axial length, but it also scales with helical radius R. Thus, it is difficult to balance these competing factors to determine *a priori* which polymorphic form will produce a larger velocity given equivalent separation distances. In the mean-field methodology, we observe that for the same helical separation distance d and field rotation rate ω, the induced background velocity from the infinite array is larger for the curly form than that of the normal form. The con-

sequence is that the self-consistent pumping angles θ^* seen in Fig. 9 are in general slightly higher than those observed in Fig. 8 for the normal form.

For a single flagellum rotating at a prescribed rate about a fixed helical axis, we measured the volumetric flow rate through a vertical plane by averaging the instantaneous rate in Eq. 9 over one rotational period. In the mean-field case we not only have an infinite number of helices, but the direction of pumping is constantly rotating. To obtain a measure of the volumetric flow rate in the case of precessional pumping, we average the instantaneous volumetric flow rate through a vertical plane normal to the azimuthal direction of the average helical axis over one epicycle ($\mathbf{r_{0,rod}}$) for the central helix as it undergoes precessional motion. We calculated the volumetric flow rate under this definition for each stable pumping angle presented in Figs. 8 and 9. Just as in the single flagellum case studied in Sec. III, we observe that the maximum volumetric flow rate occurs for those self-consistent pumping angles θ^* closest to 45°. For the normal (n=2) form with grid separation $d = 0.75L$ and Ma/Ma$_{\text{step-out}} = 0.6$ where the self-consistent pumping angle is $\theta^* = 46.41°$ as seen in Fig. 8, the volumetric flow rate per helix (non-dimensionalized in the same way as in Sec. III) is found to be $\tilde{Q} = 0.05158$; within 5% of the value of $\tilde{Q} = 0.05405$ found for the single flagellum case. This result is not surprising since the epicycles are small and the rotation rates are all below step-out, making this very similar to the single flagellum case.

To summarize, the use of the mean-field methodology allowed us to create a model which takes into account possible phase differences between flagella through a time-averaging procedure, as well as allowed for the investigation of an infinite array. We found a mechanism to control pumping for a given array separation distance by tuning the rotation rate of the underlying magnetic field to obtain specific pumping angles. We also found that a reversal of chirality, such as the one which would take place in a polymorphic transformation from the normal to curly flagellar form, would cause stable pumping solutions to switch to upright configurations and produce no net pumping. This is in contrast with the single flagellum case, where we saw that a reversal of chirality still produces pumping, but in the opposite direction. The difference in behavior arises from hydrodynamic interactions since a flagellum that produces flow in the tilt direction produces positive feedback, pushing nearby flagella in the same direction, but a flagellum of opposite handedness that produces a flow opposite the tilt direction produces negative feedback, pushing nearby flagella in the opposite direction. As discussed in Sec. I, these polymorphic transformations are an autonomous process in response to changes in external fluid parameters. Therefore, for the flagellar forest, the mean-field results predict a mechanism comparable to an "on-off switch" which may be used to regulate the flow and chemical properties of the fluid, rather than a reversal of pumping direction.
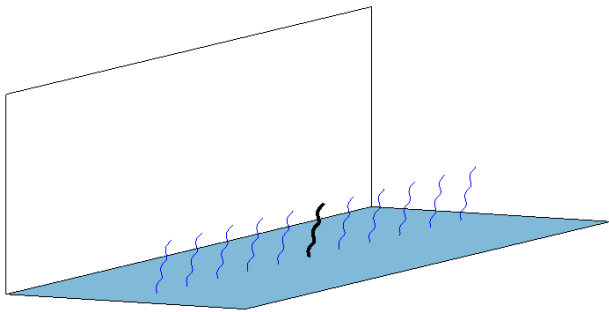
FIG. 10: A $(2D+1) \times 1$ line of helical flagella, shown here with equal tilt angle and phase. The central helix is colored black and made bold solely for emphasis in the mean-field methodology.

A. Effects of confinement

In our mean-field methodology we use precession as the requirement for self-consistent pumping for an infinite array since we believe that physically this will correspond to a fixed pumping angle in a confined channel. Confined geometries such as microchannels with rectangular cross-section are common in experimental settings. In such channels, the walls will set a preferred pumping direction, and we would not observe the precession by which we classify stability of pumping in the previous results. A simple demonstration of this effect can be seen by considering the problem of an infinite line of helices above a no-slip plane, and comparing two cases with and without a vertical wall at $x_3 = z_w$. An example of this of this geometry can be seen in Fig. 10.

We impose a slip boundary condition at the vertical wall in order to obtain a tractable problem. The solution for a Stokeslet in the presence of a no-slip plane $x_1 = 0$ and a vertical slip wall at $x_3 = z_w$ is the superposition of a regularized Blakelet above the $x_1 = 0$ plane and a regularized anti-Blakelet image mirrored across the $x_3 = z_w$ plane. This kernel is described by

$$W_{ij}^\epsilon = B_{ij}^\epsilon(\mathbf{x} - \mathbf{x}^\alpha) - B_{ij}^\epsilon(\mathbf{x} - \mathbf{x}_\mathbf{w}^\alpha), \qquad (14)$$

where $\mathbf{x}_\mathbf{w}^\alpha = \mathbf{x}^\alpha + 2z_w\hat{\mathbf{x}_3}$. In contrast, there is no exact solution for the case of a Stokeslet in an infinite microchannel bounded on four sides by no-slip walls. Thus, we use this simpler boundary condition as a proof of concept that imposing a preferred direction of flow results in stable pumping direction about an axis described by $\{\theta^*, \phi^*\}$ by replacing B_{ij}^ϵ in Eq. 8 with W_{ij}^ϵ.

As a proof of concept that wall effects change precessional solutions to single-direction pumping, we use the normal (n=2) polymorphic form at Mason number $\mathrm{Ma} = 0.994 \, \mathrm{Ma_{step\text{-}out}}$ and helix separation distance of $d = 0.85L$. First, like a two-dimensional array of helices, a line of helices without a vertical slip wall undergoes precessional motion. Then, adding the vertical wall we find a single self-consistent solution with single-direction pump-
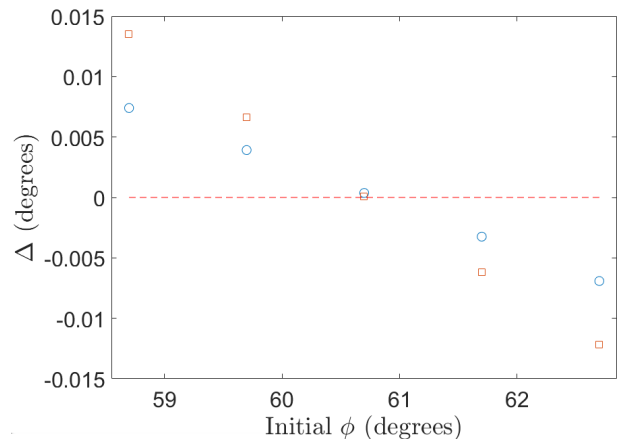

FIG. 11: Change in tilt angle $\Delta\theta$ (blue circles) and azimuthal angle $\Delta\phi$ (red squares) versus initial azimuthal angle ϕ for an initial tilt $\theta = 27.5°$. We find a stable pumping configuration for $\{\theta^*, \phi^*\} = \{27.5°, 60.7°\}$.

ing. To provide specifics, in Fig. 11, we plot the change in the tilt angle $\Delta\theta$ and azimuthal angle $\Delta\phi$ for an initial tilt $\theta = 27.5°$ over a range of initial azimuthal angles. We observe a stable configuration at $\{\theta^*, \phi^*\} = \{27.5°, 60.7°\}$. This solution has net flow through planes perpendicular to the vertical slip plane, but no net flow through planes parallel to the vertical plane.

VIII. CONCLUSIONS

Previous studies have examined the effects of tilt and phase differences on the resulting flow by way of numerical simulations which involve small finite arrays of helices with prescribed helical axes and rotation rates. These studies found that phase differences between helices are required to produce the types of flows observed in experimental work with bacterial carpets with flagella driven by bacterial motors. The importance of phase differences and an ability to examine flows generated by large arrays of flagella in microfluidic devices motivated our use of a mean-field approach which allows us to take into account phase differences through a time-averaging procedure detailed in Sec. VI A, and allows for the investigation of an infinite array through an extrapolation procedure detailed in Sec. VI B.

To summarize our results, in Sec. III we showed how the volumetric flow rate and pumping direction varies depending on helical geometry. In the single flagellum case, a reversal of rotation direction or handedness simply reverses the direction of the pumping flow. In order to better understand the pumping flows in microfluidic devices such as the flagellar forest seen in Fig. 1, we investigated the collective behavior of an infinite regular array of helical flagella driven by a magnetic torque by applying a mean-field methodology detailed in Sec. IV to find

the array separation distances and Mason numbers which give rise to self-consistent precessional pumping solutions classified by the synchronization of the flagellar tilt angle. Over the range of solutions for the normal and curly polymorphic forms, we found that the stable tilt angle decreased as the array separation distance increased or the Mason number decreased. Unlike the pumping generated by a single flagellum, we found that for an infinite array with a separation distance and Mason number which produced a non-zero stable pumping angle, a reversal of magnetic field rotation direction or handedness gives trivially stable solutions where the helices are upright and there is no net pumping. Microfluidic devices operating *in vitro* are often used within microchannel geometries which confine the flow direction. Including a vertical slip wall, we applied the mean-field methodology to show that the precessional motion observed for an infinite array is halted and a single self-consistent pumping orientation is found.

Our results have design implications for the proposed flagellar forest. We predict the ranges of flagellar lengths, separations, and frequency regimes in which the device will have on-off response to external stimuli that trigger the transformation between normal and curly forms. The fabrication method involves specifying the distance between the bead-flagella complexes by lithographically patterning the surface with an array of wells, so our results may help guide the choice of array spacing during fabrication. We expect that experiments with fabricated flagellar forests would be able to test our predictions of collective on-off switching and the parameters under which such behavior can be observed, though with the caveat that mean-field results may not be quantitatively accurate if tilt angle fluctuations are important. Furthermore, since the mean-field method finds only self-consistent solutions, it cannot predict the dynamics of the formation of predicted solutions.

The mean-field methodology presented here provides a new and valuable way to explore the collective tilt that influences pumping flows. Due to our focus on the synchronization of tilt angle, our work provides a complementary picture to previous studies of the synchronization of phase angles for rotating flagella or beating cilia and flagella [7–10, 14–17, 23–26]. For our torque-actuated rotors, we have found Mason number and geometry-dependent transitions between collectively tilted pumping phases and upright non-pumping phases.

Appendix A: Far-field decay rates and extrapolation procedures for arrays of helical filaments

The far-field velocity for a single Blakelet whose Stokeslet lies at a height h above the $x_1 = 0$ plane is given by [29]

$$u_i = \frac{f_k}{8\pi\mu}\left[\frac{12hx_1x_ix_\alpha\delta_{k\alpha}}{|\mathbf{x}|^5} + h^2\delta_{k1}\left(-\frac{(12+6\delta_{i1})x_1x_i}{|\mathbf{x}|^5} + \frac{30x_1^3x_i}{|\mathbf{x}|^7}\right)\right] \tag{A1}$$

where summation in the Einstein convention is implied. From this equation, we find the decay rates of the velocity components to be

$$u_1 \sim |\mathbf{x}|^{-5},\ u_{2,3} \sim |\mathbf{x}|^{-3}. \tag{A2}$$

The overall error between the velocity component U_i^D obtained from a $D\times D$ array and the true infinite array velocity $U_{i,\infty}^*$ is $\Delta U_i^D = |U_i^D - U_{i,\infty}^*|$. For a $D\times D$ array of flagella with separation distance d, $|\mathbf{x}| = Dd$. For large enough D, summation of the velocity components in Eq. A2 over this array give us the asymptotic decay rates of the overall error ΔU_i^D in the velocity field as

$$\Delta U_1^D \sim |Dd|^{-3},\ \Delta U_{2,3}^D \sim |Dd|^{-1}. \tag{A3}$$

Thus, we first find the time-averaged velocity at the final collocation point on the central rod, $\overline{u_j}(\mathbf{x}_{0,\mathbf{rod}}^{\alpha_N})$, similar to Eq. 13 with an additional summation to take into account the velocity induced by all the helices in the finite array of size D. We then use Richardson extrapolation for varying array size D to find the velocity for the infinite array: once we have verified that the finite arrays used to find the infinite extrapolant are sufficiently large to obey the expected power law behavior, we fit the velocity data from finite arrays assuming the errors obey the power law decay rates in Eq. A3 to find the full velocity profile along the central rod.

For example, in order to ensure that the finite arrays we use to generate the infinite array extrapolant are large enough, we examine the velocity at the central rod due to $D\times D$ finite arrays of helices with sizes 3×3 through 39×39 with a separation distance of $d = L$. In Fig. 12, we present a log-log plot of calculated array velocities at the endpoint of the central rod versus array size for $D = 11, 13, 15, 17$. We see that the asymptotic decay rates match very closely with our measured decay rates, and note that we see further improvements for larger array separation distance d. Plots such as the ones in Fig. 12 allow us to choose finite sized arrays for which we can ensure the velocity field decay rates are in the asymptotic range. To further illuminate this process, we show the velocity components at the endpoint of the central helix
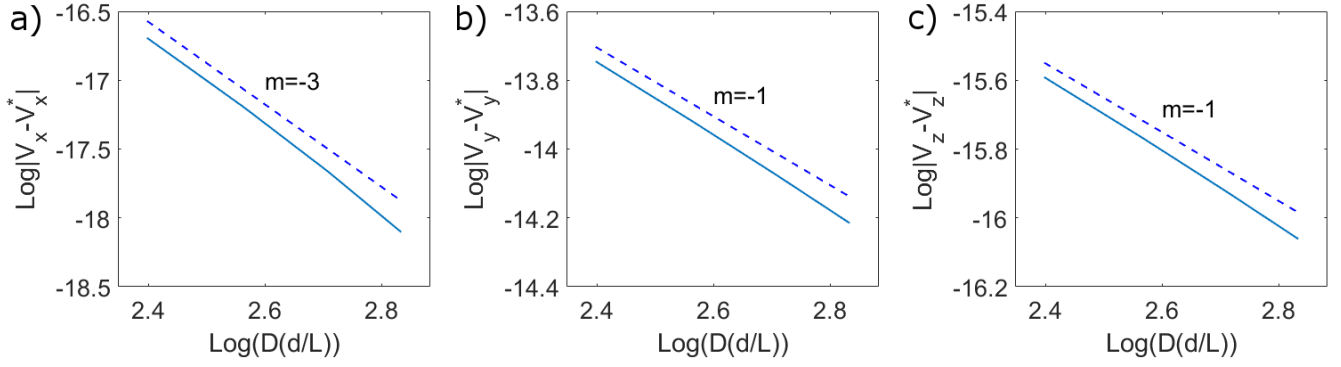
FIG. 12: Log-log plots (base e) of overall error decay rates versus array size for the (a) x- (b) y- and (c) z-component array velocities for array sizes $D = 11$, 13, 15, 17 (the solid blue lines). Decay rates from the Blakelet analysis (the blue dashed lines) are overlayed with the analytical slope from Eq. A3.
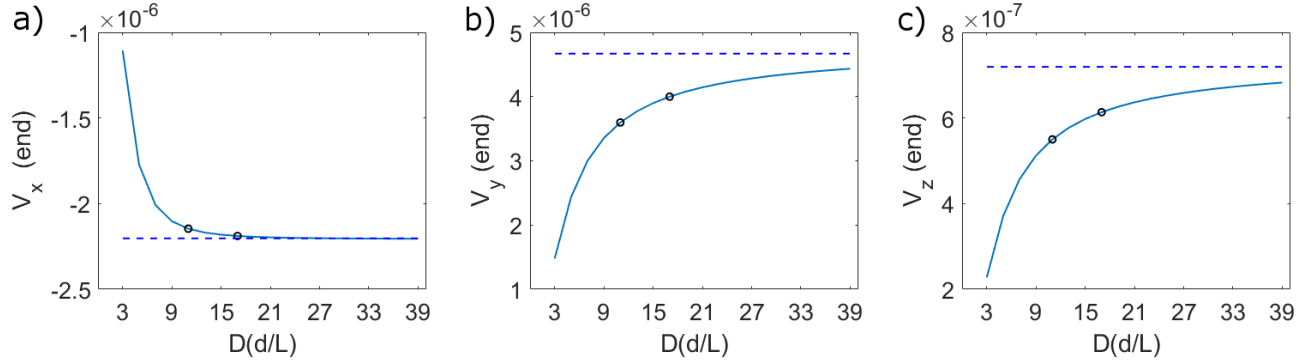

FIG. 13: Plots of (a) x- (b) y- and (c) z- component array velocities at the central helix end point for array size D ranging from 3 to 39 (the solid blue curves). Resulting infinite array extrapolation (the blue dashed lines) from the velocity components for arrays of size $D = 11$ and $D = 17$ (circled).

due to array sizes ranging from 3×3 to 39×39 in Fig. 13, that demonstrate that extrapolating infinite array results from the calculated velocity components of arrays with size 11×11 and 17×17 are sufficient to produce accurate results.

Finally, for Sec. VII A, for an infinite line of helices instead of an infinite array, the power-law decay rates of the overall error in the velocity field are changed from Eq. A3 to

$$\Delta U_1^D \sim |Dd|^{-4}, \ \Delta U_2^D \sim |Dd|^{-2}, \ \Delta U_3^D \sim |Dd|^{-4}, \tag{A4}$$

but otherwise the procedure for finding a self-consistent solution is the same as for an infinite array. Adding the vertical wall, the power-law decay rates become

$$\Delta U_1^D \sim |Dd|^{-5}, \ \Delta U_2^D \sim |Dd|^{-3}, \ \Delta U_3^D \sim |Dd|^{-5}. \tag{A5}$$

[1] R. Ghosh, G. Buxton, O. Usta, A. Balazs, and A. Alexeev, Langmuir **26**, 2963 (2009).

[2] A. Alexeev, J. Yeomans, and A. Balazs, Langmuir **24**, 12102 (2008).

[3] Z. Mills, B. Aziz, and A. Alexeev, Soft Matter **8**, 11508 (2012).

[4] H. Massoud and A. Alexeev, Soft Matter **7**, 8702 (2011).

[5] H. Shum, A. Tripathi, J. Yeomans, and A. Balazs, Langmuir **29**, 12770 (2013).

[6] A. Tripathi, H. Shum, and A. Balazs, Soft Matter **10**, 1416 (2013).

[7] D. Brumley, M. Polin, T. Pedley, and R. Goldstein, Phys. Rev. Letters **109**, 268102 (2012).

[8] D. Brumley, M. Polin, T. Pedley, and R. Goldstein, J. Roy. Soc. Interface **12**, 20141358 (2015).

[9] T. J. Pedley, D. R. Brumley, and R. E. Goldstein, J. Fluid Mech. **798**, 165 (2016).

[10] R. E. Goldstein, M. Polin, and I. Tuval, Phys. Rev. Lett.

103, 168103 (2009).

[11] S. Nonaka, S. Yoshiba, D. Watanabe, S. Ikeuchi, T. Goto, W. F. Marshall, and H. Hamada, PLOS Biology **3**, e268 (2005).

[12] D. J. Smith, J. R. Blake, and E. A. Gaffney, J. Roy. Soc. Interface **5**, 567 (2008).

[13] A. A. Smith, T. D. Johnson, D. J. Smith, and J. R. Blake, J. Fluid Mech. **705**, 26 (2012).

[14] B. Qian, H. Jiang, D. Gagnon, T. R. Powers, and K. S. Breuer, Phys. Rev. E **80**, 061919 (2009).

[15] M. Reichert and H. Stark, Eur. Phys. J. E **17**, 493 (2005).

[16] N. Uchida and R. Golestanian, Phys. Rev. Lett. **104**, 178103 (2010).

[17] E. Gauger, M. T. Downton, and H. Stark, Eur. Phys. J. E **28**, 231 (2009).

[18] N. Darnton and H. C. Berg, Biophysical Journal **92**, 2230 (2007).

[19] N. Darnton, L. Turner, S. Rojevsky, and H. C. Berg, J. Bacteriology **189**, 1756 (2007).

[20] K. Hasegawa, I. Yamashita, and K. Namba, Biophys. J. **74**, 569 (1998).

[21] Y. Ding, J. C. Nawroth, M. J. McFall-Ngai, and E. Kanso, J. Fluid Mech. **743**, 124 (2014).

[22] H. Guo, J. Nawroth, Y. Ding, and E. Kanso, Physics of Fluids **26**, 091901 (2014).

[23] N. Darnton, L. Turner, K. Breuer, and H. C. Berg, Biophysical Journal **86 (3)**, 1863 (2004).

[24] N. Uchida and R. Golestanian, Europhysics Letters **89**, 50011 (2010).

[25] K. Leiderman, E. Bouzarth, and H.-N. Nguyen, Biological Fluid Dynamics: Modeling, Computations, and Applications **628**, 73 (2014).

[26] A. L. Buchmann, L. J. Fauci, K. Leiderman, E. M. Strawbridge, and L. Zhao, "Flow induced by bacterial car-
pets and transport of microscale loads," in *Applications of Dynamical Systems in Biology and Medicine*, edited by T. Jackson and A. Radunskaya (Springer New York, New York, NY, 2015) pp. 35–53.

[27] H. C. Berg and L. Turner, Biophys. J. **65**, 2201 (1993).

[28] J. R. Blake, Proc. Camb. Phil. Soc. **70**, 303 (1971).

[29] J. R. Blake and A. T. Chwang, J. Eng. Math **8**, 23 (1974).

[30] R. Cortez, SIAM J. Sci. Comput. **23**, 1204 (2001).

[31] R. Cortez, L. Fauci, and A. Medovikov, Physics of Fluids **17**, 031504 (2005).

[32] J. Ainley, S. Durkin, R. Embid, P. Boindala, and R. Cortez, J. Computational Phys. **227**, 4600 (2008).

[33] Y. Hyon, Marcos, T. R. Powers, R. Stocker, and H. C. Fu, J. Fluid Mech. **705**, 58 (2012).

[34] J. Martindale, M. Jabbarzadeh, and H. Fu, Phys. Fluids **28**, 021901 (2016).

[35] MinJun Kim, personal communication.

[36] D. J. Smith, E. A. Gaffney, and J. R. Blake, Proc. Roy. Soc. A **465**, 2417 (2009).

[37] N. Goldenfield, *Lectures on Phase Transformations and the Renormalization Group*, 1st ed. (Perseus Books Publishing, L.L.C., Reading, Massachusetts, 1992).

[38] A. Mahoney, N. Nelson, K. Peyer, B. Nelson, and J. Abbott, Appl. Phys. Lett. **104**, 144101 (2014).

[39] K. Son, J. S. Guasto, and R. Stocker, Nature Phys. Lett. **9**, 494 (2013).

[40] J. Dauparas and E. Lauga, Phys. Rev. Fluids **1**, 043202 (2016).

[41] J. Ali, U. Cheang, J. Martindale, H. Fu, and M. Kim, submitted (2016).

[42] F. Meshkati and H. C. Fu, Phys. Rev. E **90**, 063006 (2014).

[43] H. C. Fu, M. Jabbarzadeh, and F. Meshkati, Phys. Rev. E **91**, 043011 (2015).